Article

Frequency ratio measurements at 18-digit accuracy using an optical clock network

Boulder Atomic Clock Optical Network (BACON) Collaboration*

Atomic clocks are vital in a wide array of technologies and experiments, including tests of fundamental physics[1]. Clocks operating at optical frequencies have now demonstrated fractional stability and reproducibility at the 10^{-18} level, two orders of magnitude beyond their microwave predecessors[2]. Frequency ratio measurements between optical clocks are the basis for many of the applications that take advantage of this remarkable precision. However, the highest reported accuracy for frequency ratio measurements has remained largely unchanged for more than a decade[3–5]. Here we operate a network of optical clocks based on $^{27}Al^+$ (ref. [6]), ^{87}Sr (ref. [7]) and ^{171}Yb (ref. [8]), and measure their frequency ratios with fractional uncertainties at or below 8×10^{-18}. Exploiting this precision, we derive improved constraints on the potential coupling of ultralight bosonic dark matter to standard model fields[9,10]. Our optical clock network utilizes not just optical fibre[11], but also a 1.5-kilometre free-space link[12,13]. This advance in frequency ratio measurements lays the groundwork for future networks of mobile, airborne and remote optical clocks that will be used to test physical laws[1], perform relativistic geodesy[14] and substantially improve international timekeeping[15].

Atoms serve as excellent references for the unit of time because they emit and absorb photons at well-defined resonance frequencies that are largely decoupled from environmental perturbations. Currently, the primary standard (^{133}Cs) enables realization of the second with up to 16-digit accuracy, limited by the ability to measure and control extremely fine (10 μHz level) perturbations of the microwave frequency. However, clocks based on optical transitions permit even greater control of fractional frequency perturbations by taking advantage of resonance frequencies that are 100,000 times higher than those of microwave standards. As a result, compared to primary microwave standards, clocks based on optical transitions have recently demonstrated more than a factor of 100 improvement in both frequency stability and systematic uncertainty[6–8,16,17], providing new capabilities in fundamental and applied science at the 10^{-18} level. Whereas measurements within a single laboratory between clocks based on the same atomic species have shown frequency reproducibility near this level[8,18,19], frequency ratio measurements of optical clocks based on different atomic species[3–5,20–24] lag substantially behind, with the lowest measurement uncertainty at 2.5×10^{-17}. Additionally, only one ratio, $^{199}Hg/^{87}Sr$, has been measured directly at multiple laboratories, with agreement to within the combined uncertainty of 2.0×10^{-16} (refs. [21,22]). Here, we report a network comparison of three optical clocks at the National Institute of Standards and Technology (NIST) and JILA in Boulder, Colorado, with fractional ratio uncertainties between 6×10^{-18} and 8×10^{-18}. In addition to providing a critical advance for redefining the SI second, we use these measurements to test a model of ultralight dark matter, tightening constraints on its coupling parameter to standard model fields by as much as a factor of ten over five orders of magnitude in particle mass.

The ratios reported here are (to our knowledge) the first measured using a free-space optical link, in addition to optical-fibre-based links.

A key challenge in optical clock measurements is noise from existing frequency transfer methods across very long baselines[25]. Global frequency comparisons are currently only possible using microwave frequency transfer techniques, but the state-of-the-art stability for those is near 1×10^{-15} at one day of averaging—a level achievable with optical clocks in less than a second. Although fibre-optic connections between clocks show excellent performance[11,21,26], they require fixed nodes and are limited to regional or continental networks. For these reasons, the transmission and measurement of optical clock signals through free space (the atmosphere) are essential for mobile clocks[19,27,28] and future satellite-based networks that could achieve intercontinental baselines. Such global clock networks will enable new paradigms for applications such as high-resolution geodesy[14] and tests of fundamental physics[1].

The optical network

The frequency ratio measurements presented here involve three optical atomic clocks based on the $^1S_0 \leftrightarrow {}^3P_0$ transitions in $^{27}Al^+$, ^{171}Yb and ^{87}Sr. These atomic transitions feature narrow natural linewidths (<10 mHz) at accessible laser wavelengths and are relatively insensitive to perturbation from external electric and magnetic fields[29,30]. Uncertainties due to systematic effects for these clocks have been evaluated at the 10^{-18} level and represent the current state of the art for both optical lattice clocks and single-ion clocks. These two leading technologies for optical standards differ in several ways with respect to frequency stability and systematic effects. Optical lattice clocks operate with thousands of atoms, which reduces quantum projection noise compared to that of a single ion[31], leading to intrinsically higher clock stability[8,32]. On the other hand, single-ion clocks exhibit lower intrinsic sensitivity to some environmental effects such as the Stark shift due to blackbody radiation[6]. Some of the most important parameters affecting frequency stability
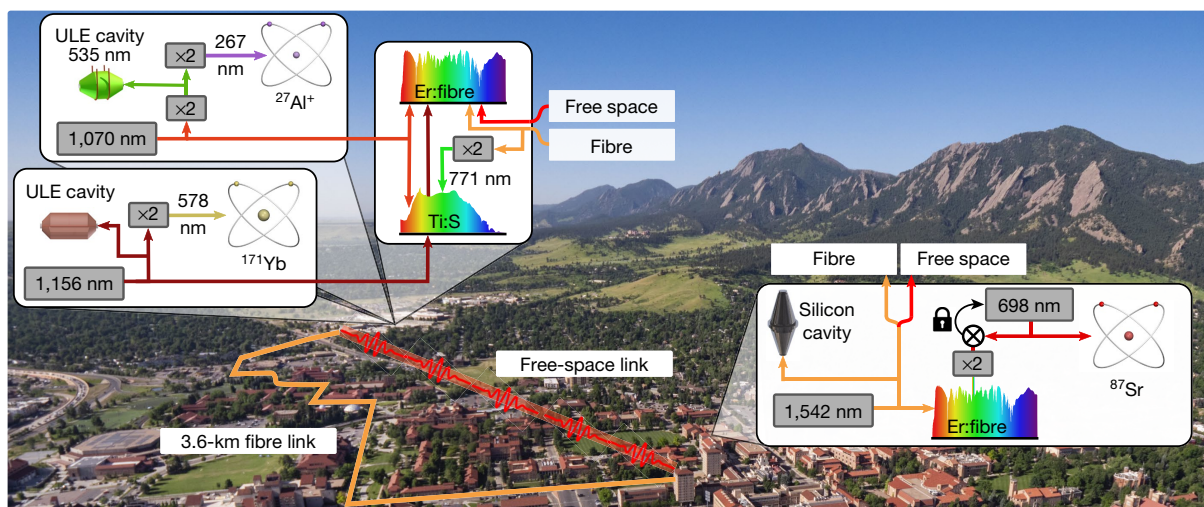
Fig. 1 | System overview of the Boulder Atomic Clock Optical Network (BACON). The photograph shows the NIST campus in the middle distance on the left, and JILA in the foreground just right of centre. Insets at top left represent two optical clocks (Al⁺ and Yb) and two optical frequency combs (Er:fibre and Ti:sapphire (Ti:S)) located on the NIST campus, while the inset at bottom right represents the Sr lattice clock located at JILA. Stabilized light from the Sr lattice clock is transferred to NIST via a 3.6-km optical fibre link (meandering orange line) for a frequency comparison with the Al⁺ and Yb clocks. The Yb and Sr lattice clocks are also compared using O-TWTFT via a 1.5-km free-space optical link (straight red line) between the two institutions. Solid coloured lines represent noise-cancelled optical links. See Methods for details of insets. ULE, ultra-low-expansion glass. Photograph taken by G. Asakawa, University of Colorado, Boulder.

and systematic effects are summarized in Extended Data Table 1, and details pertaining to the various experimental systems can be found in Methods and separate publications (Al⁺ (ref. [6]), Yb (ref. [8]) and Sr (ref. [7])).

The three optical clocks are physically separated by tens to thousands of metres and their frequencies span hundreds of THz. To cover this range of frequencies and locations, the network employs five optical frequency combs (OFCs), which provide coherent synthesis across the optical domain[33], and more than 20 phase-stabilized optical links connecting remote OFCs, lasers and optical clocks. An overview of this network is given in Fig. 1 (and a detailed schematic in Extended Data Fig. 1). The performance of network components were verified separately where possible (dashed lines in Fig. 2a). Additionally, the network contains several redundant elements to verify in real time their stability and to test for bias. For instance, two OFCs, a single-branch 180-MHz erbium-doped fibre (Er:fibre)[34] and an octave-spanning 1-GHz titanium-doped sapphire (Ti:S) OFC[35] were operated throughout the measurement campaign, yielding frequency ratios that agreed at the 5×10^{-19} level.

Local to each clock, a laser is pre-stabilized to a high-finesse optical reference cavity, which provides short-term stability and a linewidth sufficiently narrow to probe the clock transition. The optical clock transition wavelengths near 267 nm, 578 nm and 698 nm are coherently connected to infrared lasers at 1,070 nm, 1,156 nm and 1,542 nm, respectively, which are delivered to the measurement OFCs at NIST via optical fibres with active phase noise cancellation[2]. For the Sr clock, an OFC local to JILA phase-coherently links a silicon-cavity-stabilized laser at 1,542 nm to a separate clock laser at 698 nm, which ultimately probes the clock transition[32]. The use of a 1,542-nm laser is convenient, as this wavelength experiences low losses in fibre and is transmitted from JILA to NIST over the longest fibre link in the network (3.6 km)[11]. In all cases, slow feedback (<1 Hz bandwidth) based on interrogation of the atomic clock transition with each local oscillator stabilizes the infrared laser to the atomic resonance.

In addition to the fibre-based connections between clocks, the network employs a free-space link between JILA and NIST. Optical two-way time-frequency transfer (O-TWTFT) is used to measure the Yb/Sr ratio across this link. Laser light stabilized by the Sr and Yb clocks is transmitted via noise-cancelled fibres to OFCs located within transceivers at either end of the free-space optical link. OFC pulses from each transceiver are exchanged across the link. Because the sampled air paths are common to pulse trains travelling in each direction, O-TWTFT allows for frequency transfer at better than 10^{-18} instability despite the presence of kilometre-length turbulent air paths[12,36]. Simultaneous measurements of the Yb/Sr ratio using the free-space and fibre links test the network independently of the clocks. The O-TWTFT system was operated for 6 days in conjunction with the rest of the network during the measurement campaign in 2018. (Details of the free-space-based measurements can be found in ref. [13]). For those 6 days, the uptimes and thus statistical uncertainties were essentially the same for both the free-space-based and fibre-based measurements of the Yb/Sr ratio. The free-space O-TWTFT system did not operate on 23 March owing to a day-long snowstorm, or on 16 February or 14 June due to limited physical access at JILA. When restricted to common measurement times, the weighted mean of the difference in ratios obtained by the two links is $(-4.5 \pm 6.1) \times 10^{-19}$ (ref. [13]).

Results

The clock comparison spanned November 2017 through to June 2018. An example of the measurement stability, $\sigma(\tau)$, observed on a single day is given in Fig. 2a. The data are observed to follow white frequency noise statistics, $\sigma(\tau) = \sigma_0/\sqrt{\tau}$ (where τ is in s), for averaging periods τ greater than 100 s. A fit of the instability at 1 s, σ_0, to the data in Fig. 2a yields $3.1(2) \times 10^{-16}$ for the Yb/Sr ratio, and $1.3(1) \times 10^{-15}$ for the Al⁺/Yb and Al⁺/Sr ratios. Uncertainty due to measurement instability on each day was calculated by extrapolating this fit to the duration of the full dataset. Analysis of the ratio data treats individual measurement days as separate because some operating conditions, which affected measurement stability and systematic shifts, varied between days. Day-by-day measurements of each ratio (Fig. 2b–d) were corrected from their laboratory operational conditions to the perturbation-free ideal at zero electric and magnetic field, absolute zero temperature, and to a common gravitational potential[37].

For the three ratios, we observe various degrees of scatter compared to what is expected from the statistical uncertainties alone. Specifically, Al/Sr measurements are under-scattered relative to the statistical
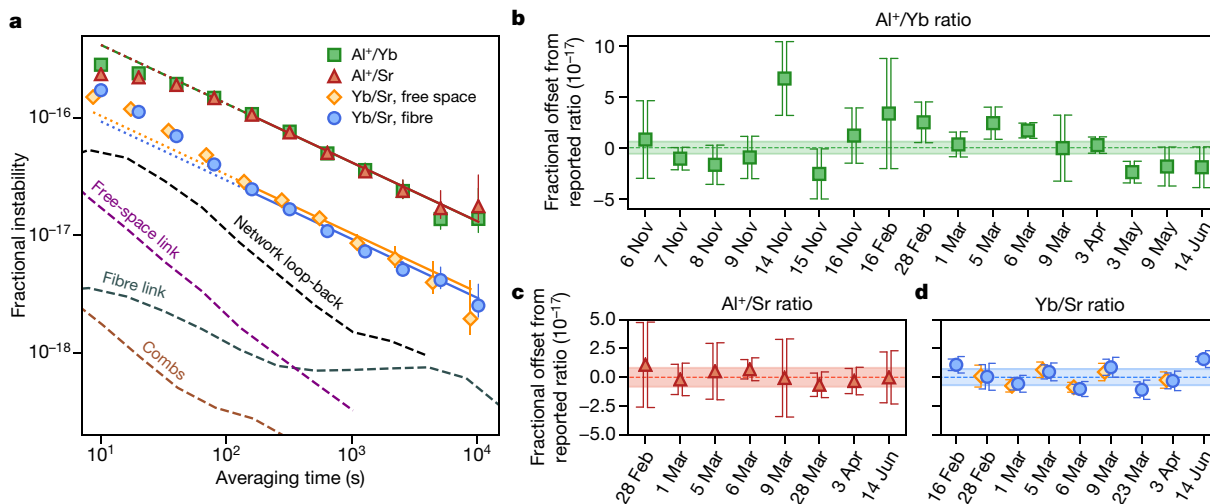
Fig. 2 | Ratio measurement results. a, Fractional instability in the ratio measurements (points; see key) and network components (labelled dashed lines) as a function of averaging time. The plot shows the instability of the free-space and fibre links between JILA and NIST, the optical frequency combs used in the measurement, and a loop-back test over both the fibre and free-space links through several of the laboratories at NIST and JILA. All data are analysed using the overlapping Allan deviation. Matching lines to the ratio data are weighted fits using a white frequency noise model, beginning at a 100-s averaging time. Error bars indicate 68% confidence intervals.

b–**d**, Frequency ratio measurements taken from November 2017 to June 2018, displayed as a fractional offset from their final reported values. In **d**, measurements using both fibre (blue) and free-space (orange) frequency transfer are shown. Error bars to the left side of each data point represent statistical uncertainty, whereas error bars on the right represent the quadrature sum of statistical and systematic uncertainties. Lightly shaded regions correspond to the final uncertainty (1 standard deviation) of each ratio: 5.9×10^{-18}, 8.0×10^{-18} and 6.8×10^{-18}, for Al$^+$/Yb, Al$^+$/Sr and Yb/Sr, respectively.

error bars while the Yb/Sr and Al/Yb measurements both exhibit some degree of excess scatter. To deal with excess scatter and evaluate the measurement uncertainties rigorously in a common framework, we developed a comprehensive Bayesian model for each ratio (see Methods and Extended Data Fig. 3). The model incorporates uncertainty due to the known statistical and systematic effects but also allows for unknown effects that may vary between days[38,39]. This daily variation is assumed to be normally distributed about a zero mean. Detailed models for each ratio, including prior and posterior probability distributions for the expected values and between-day variability, are given in Supplementary Information. The main results of this analysis are: (1) agreement of the consensus ratio values with the weighted means from a simplified analysis (see Methods); (2) a more conservative estimate of the final ratio uncertainties compared to a standard analysis based on χ^2 statistics (Extended Data Table 3); and (3) credible intervals for the between-day variability ξ (see Extended Data Table 2).

Based on the results of the comprehensive Bayesian model, the frequency ratios, ν_k/ν_l, and their uncertainties, corresponding to the standard deviations of the posterior distributions, are:

$$\nu_{Al^+}/\nu_{Yb} = 2.162887127516663703(13),$$

$$\nu_{Al^+}/\nu_{Sr} = 2.611701431781463025(21),$$

$$\nu_{Yb}/\nu_{Sr} = 1.2075070393433378482(82).$$

Although the final fractional uncertainties are comparable for all ratios, the statistical and systematic effects that contribute to each one are distinct (Extended Data Table 3).

Al$^+$/Yb. This ratio uncertainty is dominated by measurement instability, primarily due to quantum projection noise of the single Al$^+$ ion. The reduced-χ^2 value $\chi^2_{red} = 1.5$ (see Methods), which quantifies scatter in the data relative to statistical error bars, is only marginally significant (probability $P = 0.1$ of observing a value higher than this by statistical fluctuations alone). The combined uncertainty due to systematic effects of 2.2×10^{-18} has a minor effect on the final ratio uncertainty.

Al$^+$/Sr. The uncertainty in this ratio has approximately equal contributions from clock instability and the total uncertainty due to systematic effects (5.1×10^{-18}). Although the ratio data appear to be underscattered $\left(\chi^2_{red} = 0.2\right)$, the comprehensive Bayesian model still includes a term for between-day fluctuations, which increases the final uncertainty compared to the evaluation based on the standard error.

Yb/Sr. Short-term measurement instability contributes negligibly to the total uncertainty in this ratio such that day-to-day scatter ($\chi^2_{red} = 6.0$, based on statistical error only), which can be resolved due to the lower quantum projection noise of the optical lattice clocks, is the dominant statistical uncertainty. However, the largest contribution to the total uncertainty of this ratio is the combined uncertainty due to systematic effects of 5.2×10^{-18}.

For perfectly overlapping data, we expect the closure relation, $C \equiv \left(\frac{\nu_{Al^+}}{\nu_{Yb}}\right)\left(\frac{\nu_{Sr}}{\nu_{Al^+}}\right)\left(\frac{\nu_{Yb}}{\nu_{Sr}}\right) = 1$. Owing to non-overlapping data, we find $C - 1 = 6 \times 10^{-19}$, which is less than the combined statistical uncertainty, 8.5×10^{-18}, taken as the quadrature sum of statistical uncertainties of the three ratios in Extended Data Table 3. The overlapping data do provide an opportunity to test for the source of daily fluctuations in the clock ratios (see Methods and Extended Data Fig. 4), but statistical uncertainties of the few overlapping days make that result inconclusive.

Discussion

These measurements are the first reported frequency ratios with fractional uncertainties below 1×10^{-17}. Figure 3a–c compares our measured ratio values with previous frequency ratio measurements. For all ratios, we observe consistency with CIPM (International Committee for Weights and Measures) recommended clock frequency values[15]. Only the Yb/Sr ratio has been previously measured via optical comparison; our result is in agreement with the weighted mean of all the previous optical measurements within 1.7σ (where σ is the standard error of the weighted mean). In the calculation of this mean and uncertainty we assume no correlation in the measurements contributing to these ratios, an assumption that needs careful consideration as more ratios
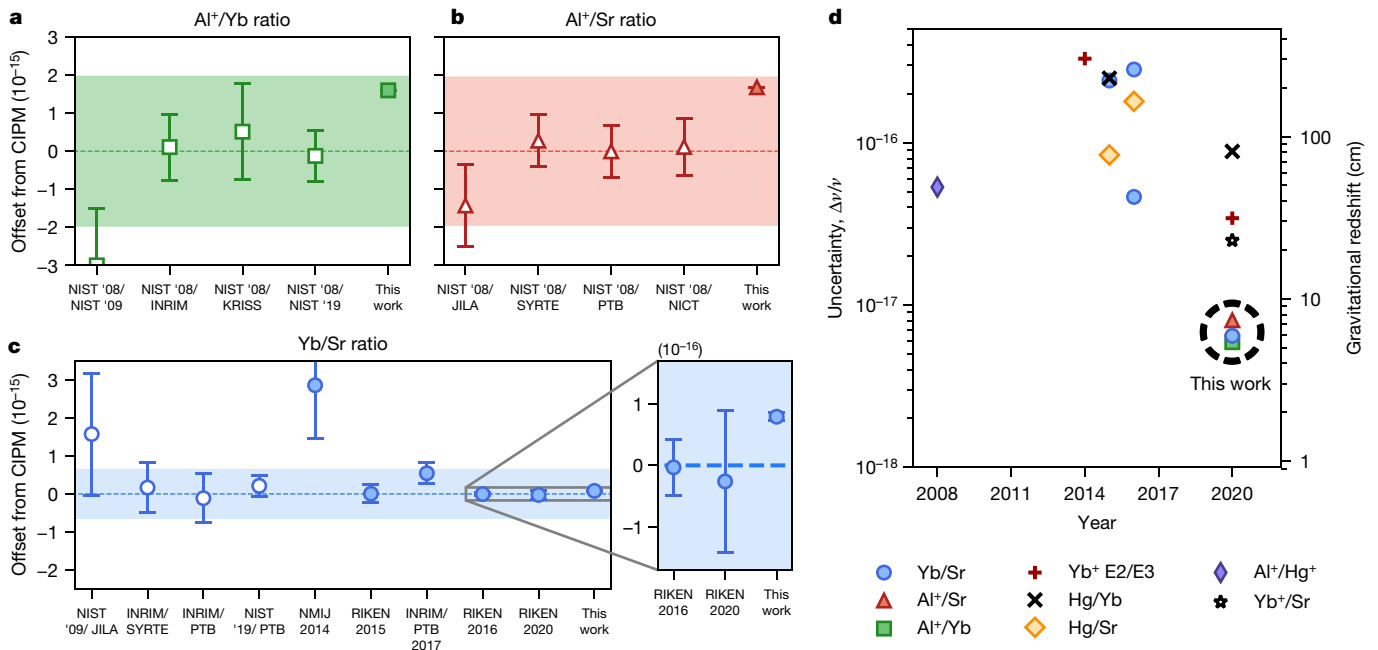
Fig. 3 | Comparison of measured frequency ratios with previous results.
a–**c**, Values of ratios Al⁺/Yb (**a**), Al⁺/Sr (**b**) and Yb/Sr (**c**), reported as fractional offsets from the ratios of current CIPM recommended frequencies (Al⁺, 1121015393207857.3 Hz; Yb, 518295836590863.6 Hz; and Sr, 429228004229873.0 Hz, with fractional uncertainties of 1.9×10^{-15}, 5×10^{-16} and 4×10^{-16}, respectively)[15]. The shaded region in each plot indicates the standard uncertainty of the CIPM ratio, determined from the quadrature sum of the absolute frequency uncertainties. Ratios based on absolute frequency measurements are presented with open symbols, whereas frequency ratios based only on optical clock measurements are presented with filled symbols. For Yb/Sr (**c**), a subset of the most accurate absolute frequency measurements is displayed[44–49] in addition to all direct optical frequency ratios[4,21,28,50], and an indirect ratio via Hg (ref. [23]). The inset focuses on the three most accurate measurements to date. For the ratios involving Al⁺ (**a**, **b**), there are no other direct optical measurements against Sr or Yb, so all prior data are based on absolute frequency measurements[3,40,51,52]. All error bars indicate 1 standard deviation. References for abbreviations, listed in order of first use from left to right in **a**–**c**, are: NIST '08[3,40]; NIST '09[45]; INRIM[46]; KRISS[52]; NIST '19[49]; JILA[44]; SYRTE[47]; PTB[48]; NICT[51]; NMIJ 2014[50]; RIKEN 2015[21]; INRIM/PTB 2017[28]; RIKEN 2016[4]; RIKEN 2020[23]. **d**, Fractional ratio measurement uncertainties including previous direct optical ratio results[3,4,20–22,28] as a function of year. The right-hand vertical axis indicates how measurement uncertainty correlates to differential height sensitivity in the gravitational redshift. Yb⁺ E2/E3 refers to electric quadrupole and electric octupole transitions in this ion.

are measured. The previous ratios that include Al⁺ all rely on an optical comparison with the Hg⁺ optical clock[3] combined with an absolute frequency measurement of the Hg⁺ clock[40], which strongly correlates these previous ratios. For both Al⁺/Sr and Al⁺/Yb, we observe a significant difference from those previous ratios with discrepancies as high as 3σ based on their combined uncertainties. We have not been able to identify the source of these discrepancies based on evaluations of the current systems, but we note that the uncertainties in previous measurements are much larger than the current measurements owing to statistical noise and systematic effects in the caesium standards. Figure 3d shows the fractional measurement uncertainties for previous ratio measurements that are based on the direct comparison of optical clocks. The right-hand vertical axis puts this in the context of relativistic geodesy, showing the geodetic height sensitivity close to the surface of Earth for a given measurement uncertainty. The measurement precision realized in this work now provides access to centimetre-level resolution in relativistic geodesy.

In addition to their use in metrology, frequency ratios of optical clocks are sensitive probes of physics beyond the standard model. Some models postulate dark matter composed of ultralight bosonic particles (mass, m_ϕ) that cause apparent oscillations in the fundamental constants at the particle's Compton frequency, $\omega_C = m_\phi c^2 / \hbar$, where $2\pi\hbar$ is Planck's constant and c is the speed of light in vacuum[1]. Atomic clock frequency ratios are sensitive to changes in fundamental constants and thus well suited to study this class of dark-matter models. Here we evaluate all ratio data between optical clocks at NIST/JILA, including the earlier comparison of the Al⁺ and Hg⁺ clocks[3,41], to

establish new constraints on the modulus, d_e, describing the coupling of dark matter to the electromagnetic tensor (Fig. 4). The sensitivity of atomic frequency ratios to apparent variation in fundamental constants arises from relativistic effects in each clock atoms' atomic structure[1]. As a result, the sensitivity factors for Yb ($K_{Yb} = 0.31$) and Hg⁺ ($K_{Hg^+} = -2.9$) are higher than those of Al⁺ ($K_{Al^+} = 0.008$) and Sr ($K_{Sr} = 0.06$). Although the Al⁺/Hg⁺ data benefits from 10× higher intrinsic sensitivity compared to the two Yb ratios, the stability of the new measurements establish competitive constraints, particularly for Yb/Sr in the higher-mass range. The overall constraints are improved by as much as an order of magnitude across five orders of magnitude in particle mass compared to previous constraints[9,10].

Conclusion

The stringent constraint on a model of dark matter is one example of the valuable data provided by optical clock frequency ratios. Optical clock ratios have also been used to search for drifts in the fundamental constants[3,20] and to test relativity theory[18,19]. We anticipate these data and future measurements like it will continue to provide information to test theories beyond the standard model. The two-way optical free-space link between NIST and JILA is the first to be used in a high-accuracy optical clock comparison to date, and similar systems will be necessary for optical clock applications, such as relativistic geodesy[14], that require ultrastable optical networks to extend beyond the reach of fibre-optic links. Establishment of an accurate and stable global network based on both free-space and fibre-optic links will be critical in the eventual
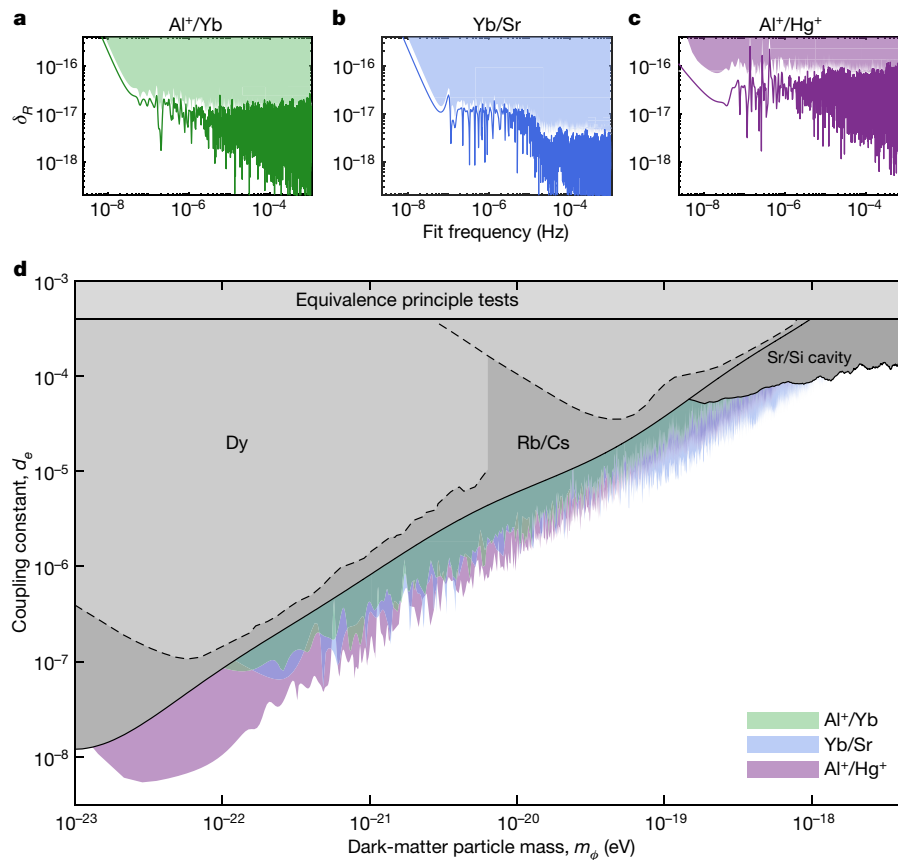
Fig. 4 | Constraints on ultralight dark matter. a–c, Amplitude spectra resulting from fits of the model $\delta_R\sin(\omega_C t + \theta) + \delta_{R,0}$ to the ratio time-series data. Here δ_R is the fit amplitude, ω_C is the dark-matter particle Compton frequency, θ is an unknown phase and $\delta_{R,0}$ is a constant offset. The fit frequency corresponds to $\omega_C/2\pi$ and shaded regions are excluded in the fit at 95% confidence. **d**, Exclusion plot for ultralight bosonic dark matter. Previous constraints reproduced from refs. [9,10,66] rely on equivalence principle tests (horizontal black line), frequency measurements with atomic dysprosium (Dy, dashed black curves), frequency ratio measurements between microwave atomic clocks based on Rb and Cs (Rb/Cs, solid black curve) and comparisons between an Sr optical lattice clock and a silicon cryogenic optical cavity (Sr/Si

cavity, solid black curve in top right). To compare with bounds set by the latter data, we assume the dark-matter particle of mass m_ϕ couples only through the parameter d_e, which affects the fine-structure constant. All bounds derived from atomic spectroscopy are modified by the same scaling factor to account for stochastic fluctuations in the dark-matter field amplitude[53]. Bounds derived from equivalence principle tests are not affected. Grey-shaded regions exclude coupling constants higher than the bound shown at 95% confidence for each constraint. Not shown are astrophysical constraints that favour masses above 10^{-22} eV corresponding to a particle with wavelength on the scale of a dwarf galaxy, about 10 kpc (ref. [54]).

redefinition and dissemination of an optical second, as anticipated by metrology institutes worldwide[42,43].

Online content

Any methods, additional references, Nature Research reporting summaries, source data, extended data, supplementary information, acknowledgements, peer review information; details of author contributions and competing interests; and statements of data and code availability are available at https://doi.org/10.1038/s41586-021-03253-4.

1. Safronova, M. S. et al. Search for new physics with atoms and molecules. *Rev. Mod. Phys.* **90**, 025008 (2018).
2. Ludlow, A. D., Boyd, M. M., Ye, J., Peik, E. & Schmidt, P. O. Optical atomic clocks. *Rev. Mod. Phys.* **87**, 637–701 (2015).
3. Rosenband, T. et al. Frequency ratio of Al⁺ and Hg⁺ single-ion optical clocks; metrology at the 17th decimal place. *Science* **319**, 1808–1812 (2008).
4. Nemitz, N. et al. Frequency ratio of Yb and Sr clocks with 5 × 10⁻¹⁷ uncertainty at 150 seconds averaging time. *Nat. Photon.* **10**, 258–261 (2016).
5. Dörscher, S. et al. Optical frequency ratio of a ¹⁷¹Yb⁺ single-ion clock and a ⁸⁷Sr lattice clock. Preprint at https://arXiv.org/abs/2009.05470 (2020).
6. Brewer, S. M. et al. An ²⁷Al⁺ quantum-logic clock with systematic uncertainty below 10⁻¹⁸. *Phys. Rev. Lett.* **123**, 033201 (2019).
7. Bothwell, T. et al. JILA SrI optical lattice clock with uncertainty of 2.0 × 10⁻¹⁸. *Metrologia* **56**, 065004 (2019).
8. McGrew, W. F. et al. Atomic clock performance enabling geodesy below the centimetre level. *Nature* **564**, 87–90 (2018).
9. Van Tilburg, K., Leefer, N., Bougas, L. & Budker, D. Search for ultralight scalar dark matter with atomic spectroscopy. *Phys. Rev. Lett.* **115**, 011802 (2015).
10. Hees, A., Guéna, J., Abgrall, M., Bize, S. & Wolf, P. Searching for an oscillating massive scalar field as a dark matter candidate using atomic hyperfine frequency comparisons. *Phys. Rev. Lett.* **117**, 061301 (2016).
11. Foreman, S. M. et al. Coherent optical phase transfer over a 32-km fiber with 1s instability at 10⁻¹⁷. *Phys. Rev. Lett.* **99**, 153601 (2007).
12. Sinclair, L. C. et al. Comparing optical oscillators across the air to milliradians in phase and 10⁻¹⁷ in frequency. *Phys. Rev. Lett.* **120**, 050801 (2018).
13. Bodine, M. I. et al. Optical atomic clock comparison through turbulent air. Preprint at https://arXiv.org/abs/2006.01306 (2020).
14. Mehlstäubler, T. E., Grosche, G., Lisdat, C., Schmidt, P. O. & Denker, H. Atomic clocks for geodesy. *Rep. Prog. Phys.* **81**, 064401 (2018).
15. Riehle, F., Gill, P., Arias, F. & Robertsson, L. The CIPM list of recommended frequency standard values: guidelines and procedures. *Metrologia* **55**, 188–200 (2018).
16. Nicholson, T. L. et al. Systematic evaluation of an atomic clock at 2 × 10⁻¹⁸ total uncertainty. *Nat. Commun.* **6**, 6896 (2015).
17. Huntemann, N., Sanner, C., Lipphardt, B., Tamm, Chr. & Peik, E. Single-ion atomic clock with 3 × 10⁻¹⁸ systematic uncertainty. *Phys. Rev. Lett.* **116**, 063001 (2016).
18. Sanner, C. et al. Optical clock comparison for Lorentz symmetry testing. *Nature* **567**, 204–208 (2019).
19. Takamoto, M. et al. Test of general relativity by a pair of transportable optical lattice clocks. *Nat. Photon.* **14**, 411–415 (2020).
20. Godun, R. M. et al. Frequency ratio of two optical clock transitions in ¹⁷¹Yb⁺ and constraints on the time variation of fundamental constants. *Phys. Rev. Lett.* **113**, 210801 (2014).
21. Takamoto, M. et al. Frequency ratios of Sr, Yb, and Hg based optical lattice clocks and their applications. *C.R. Phys.* **16**, 489–498 (2015).

22. Tyumenev, R. et al. Comparing a mercury optical lattice clock with microwave and optical frequency standards. *New J. Phys.* **18**, 113002 (2016).

23. Ohmae, N., Bregolin, F., Nemitz, N. & Katori, H. Direct measurement of the frequency ratio for Hg and Yb optical lattice clocks and closure of the Hg/Yb/Sr loop. *Opt. Express* **28**, 15112–15121 (2020).

24. Lange, R. et al. Improved limits for violations of local position invariance from atomic clock comparisons. Preprint at https://arXiv.org/abs/2010.06620 (2020).

25. Riehle, F. Optical clock networks. *Nat. Photon.* **11**, 25–31 (2017).

26. Lisdat, C. et al. A clock network for geodesy and fundamental science. *Nat. Commun.* **7**, 12443 (2016).

27. Delehaye, M. & Lacroûte, C. Single-ion, transportable optical atomic clocks. *J. Mod. Opt.* **65**, 622–639 (2018).

28. Grotti, J. et al. Geodesy and metrology with a transportable optical clock. *Nat. Phys.* **14**, 437–441 (2018).

29. Dehmelt, H. G. Monoion oscillator as potential ultimate laser frequency standard. *IEEE Trans. Instrum. Meas.* **IM-31**, 83–87 (1982).

30. Hall, J. L., Zhu, M. & Buch, P. Prospects for using laser-prepared atomic fountains for optical frequency standards applications. *J. Opt. Soc. Am. B* **6**, 2194–2205 (1989).

31. Itano, W. M. et al. Quantum projection noise: population fluctuations in two-level systems. *Phys. Rev. A* **47**, 3554–3570 (1993).

32. Oelker, E. et al. Demonstration of 4.8×10^{-17} stability at 1s for two independent optical clocks. *Nat. Photon.* **13**, 714–719 (2019).

33. Fortier, T. & Baumann, E. 20 years of developments in optical frequency comb technology and applications. *Commun. Phys.* **2**, 153 (2019); correction **3**, 85 (2020).

34. Leopardi, H. et al. Single-branch Er:fiber frequency comb for precision optical metrology with 10^{-18} fractional instability. *Optica* **4**, 879–885 (2017).

35. Fortier, T. M., Bartels, A. & Diddams, S. A. Octave-spanning Ti:sapphire laser with a repetition rate >1 GHz for optical frequency measurements and comparisons. *Opt. Lett.* **31**, 1011–1013 (2006).

36. Deschênes, J.-D. et al. Synchronization of distant optical clocks at the femtosecond level. *Phys. Rev. X* **6**, 021016 (2016).

37. van Westrum, D. *Geodetic Survey of NIST and JILA Clock Laboratories*. NOAA Technical Report NOS NGS 77 (NOAA, 2019).

38. Gelman, A. et al. *Bayesian Data Analysis* 3rd edn (Chapman & Hall/CRC Texts in Statistical Science) (CRC Press, 2014).

39. Koepke, A., Lafarge, T., Possolo, A. & Toman, B. Consensus building for interlaboratory studies, key comparisons, and meta-analysis. *Metrologia* **54**, S34–S62 (2017).

40. Stalnaker, J. E. et al. Optical-to-microwave frequency comparison with fractional uncertainty of 10^{-15}. *Appl. Phys. B* **89**, 167–176 (2007).

41. Rosenband, T. et al. Alpha-dot or not: comparison of two single atom optical clocks. In *Proceedings of the 7th Symposium on Frequency Standards and Metrology* (ed. Maleki, L.) 20–33 (World Scientific, 2009).

42. Riehle, F. Towards a redefinition of the second based on optical atomic clocks. *C.R. Phys.* **16**, 506–515 (2015).

43. Gill, P. When should we change the definition of the second? *Phil. Trans. R. Soc. A* **369**, 4109–4130 (2011).

44. Campbell, G. K. et al. The absolute frequency of the ^{87}Sr optical clock transition. *Metrologia* **45**, 539–548 (2008).

45. Lemke, N. D. et al. Spin-1/2 optical lattice clock. *Phys. Rev. Lett.* **103**, 063001 (2009).

46. Pizzocaro, M. et al. Absolute frequency measurement of the $^1S_0$–$^3P_0$ transition of ^{171}Yb. *Metrologia* **54**, 102–112 (2017).

47. Lodewyck, J. et al. Optical to microwave clock frequency ratios with a nearly continuous strontium optical lattice clock. *Metrologia* **53**, 1123–1130 (2016).

48. Grebing, C. et al. Realization of a timescale with an accurate optical lattice clock. *Optica* **3**, 563–569 (2016).

49. McGrew, W. F. et al. Towards the optical second: verifying optical clocks at the SI limit. *Optica* **6**, 448–454 (2019).

50. Akamatsu, D. et al. Frequency ratio measurement of ^{171}Yb and ^{87}Sr optical lattice clocks. *Opt. Express* **22**, 7898–7905 (2014).

51. Hachisu, H., Petit, G., Nakagawa, F., Hanado, Y. & Ido, T. SI-traceable measurement of an optical frequency at the low 10^{-16} level without a local primary standard. *Opt. Express* **25**, 8511–8523 (2017).

52. Kim, H. et al. Improved absolute frequency measurement of the ^{171}Yb optical lattice clock at KRISS relative to the SI second. *Jpn. J. Appl. Phys.* **56**, 050302 (2017).

53. Centers, G. P. et al. Stochastic fluctuations of bosonic dark matter. Preprint at https://arXiv.org/abs/1905.13650 (2019).

54. Hui, L., Ostriker, J. P., Tremaine, S. & Witten, E. Ultralight scalars as cosmological dark matter. *Phys. Rev. D* **95**, 043541 (2017).

Boulder Atomic Clock Optical Network (BACON) Collaboration*

Kyle Beloy[1], Martha I. Bodine[1], Tobias Bothwell[2], Samuel M. Brewer[1,5], Sarah L. Bromley[2,6], Jwo-Sy Chen[1,3,7], Jean-Daniel Deschênes[4], Scott A. Diddams[1,3], Robert J. Fasano[1,3], Tara M. Fortier[1]✉, Youssef S. Hassan[1,3], David B. Hume[1]✉, Dhruv Kedar[2], Colin J. Kennedy[1,2]✉, Isaac Khader[1], Amanda Koepke[1]✉, David R. Leibrandt[1,3], Holly Leopardi[1,3,8]✉, Andrew D. Ludlow[1], William F. McGrew[1,3], William R. Milner[2], Nathan R. Newbury[1], Daniele Nicolodi[1,3], Eric Oelker[1,2], Thomas E. Parker[1], John M. Robinson[2], Stefania Romisch[1,9], Stefan A. Schäffer[1,10], Jeffrey A. Sherman[1], Laura C. Sinclair[1]✉, Lindsay Sonderhouse[2], William C. Swann[1], Jian Yao[1], Jun Ye[1,2,3] & Xiaogang Zhang[1,3]✉

[1]National Institute of Standards and Technology, Boulder, CO, USA. [2]JILA, University of Colorado, Boulder, CO, USA. [3]Department of Physics, University of Colorado, Boulder, CO, USA. [4]Consultation OctoSig Inc., Quebec City, Quebec, Canada. [5]Present address: Department of Physics, Colorado State University, Fort Collins, CO, USA. [6]Present address: Department of Physics, Durham University, Durham, UK. [7]Present address: IonQ Inc., College Park, MD, USA. [8]Present address: Space Dynamics Laboratory, North Logan, UT, USA. [9]Present address: Northrup Grumman Mission Systems, Woodland Hills, CA, USA. [10]Present address: Van der Waals-Zeeman Institute, Institute of Physics, University of Amsterdam, Amsterdam, The Netherlands. ✉e-mail: tara.fortier@nist.gov; david.hume@nist.gov; colin.kennedy@colorado.edu; amanda.koepke@nist.gov; holly.leopardi@colorado.edu; laura.sinclair@nist.gov; xiaogang.zhang@nist.gov

Article

Methods

Details of the ratio calculations are given in Supplementary Information, while the design, operating conditions and evaluation of systematic effects of the three optical clocks involved in these measurements are described in detail in separate publications[6–8] (relevant parameters summarized in Extended Data Table 1). The uncertainty budget is summarized in Extended Data Table 3. Below, we describe some considerations relevant for the specific operating conditions during the measurement campaign.

Al⁺ single-ion clock

The systematic effects detailed in ref. [6] represent the operating condition of the clock during the last few months of this measurement campaign. Early in the measurement campaign, we observed two effects that caused additional uncertainty in the clock frequency.

First, a linear Doppler shift was observed as an offset (-5 × 10⁻¹⁷) in the line centres measured from two counterpropagating probe lasers. This is suppressed in all of the data by averaging the direction-dependent error signals, but angular deviation and contrast imbalance between the two probe directions make this cancellation imperfect[6]. The angular deviation was minimized—beginning in the data from 16 February 2018—by coupling the two counterpropagating beams through the same optical fibre. The effect of the contrast imbalance was eliminated by introducing a differential servo for the two probe directions, which was implemented beginning with the data from 28 March 2018.

Second, some data were affected by phase slips in the phase-locked loops used for cancelling Doppler noise of the optical fibres[11,55,56]. To prevent a bias in the measured frequency ratio, we remove ratio data 10 s before and 100 s after any observed outliers in the fibre-noise counters. We place bounds on the residual uncertainty due to these events by modelling their impact as an impulse response of the clock servo based on an observed $5(2) \times 10^{-17}$ shift after the phase-slip. This gives 3×10^{-19} as an upper bound on the uncertainty, which is further suppressed during the uninterrupted lock period. Nevertheless, this uncertainty is applied to all of the data which had more than 5% of the data removed owing to glitches (corresponding to an average of 1.6 phase-slips detected per hour).

Sr optical lattice clock

This work employed the JILA SrI clock system instead of the SrII system[16]. The SrI clock was previously evaluated with an uncertainty due to systematic effects of 5×10^{-17}, and was improved before, throughout and after this work. As a result, there are four differences between the evaluation detailed in ref. [7] and that demonstrated here.

First, in ref. [7] the density shift was carefully controlled for day-to-day reproducibility with an uncertainty of 4×10^{-19}. However, here the atomic density shift was evaluated on each comparison day, yielding a mean density shift coefficient ranging between -1.71×10^{-17} and -3.57×10^{-17} per 1,000 atoms, with each determination having measurement-limited statistical uncertainty between 1.3×10^{-18} and 3.2×10^{-18} per 1,000 atoms. Corrections for the density shift are made point-by-point using the measured atom number on each experimental cycle. The average shift and associated uncertainty applied to each point on a given day is given in Supplementary Table 3. The stability of this frequency correction over the course of a single day is supported by the reproducibility of the shift between multiple evaluations over many hours and the white noise character of the concatenated data taken hours apart. The average atom number varies between days, ranging from 1,000 to 2,700. The uncertainty of these frequency corrections are statistically limited by each day's evaluation of the density shift coefficient and as such are added in quadrature with the statistical uncertainty for each day's ratio measurement. The total contribution of the Sr density shift uncertainty to the systematic error budget in Supplementary Table 3 is 1.0×10^{-18} for both the Yb/Sr and Al⁺/Sr ratios.

Second, the lattice light shift uncertainty is higher than that reported in ref. [7]. In the present work, two different lattice wavelengths are used, one for all the data up to the last day and then—after replacing the 532-nm pump laser for the Ti:sapphire which supplies 813-nm trapping light—a different wavelength for the last comparison day. For the first wavelength, six independent evaluations of the lattice light shift were undertaken over the course of four months, producing an uncertainty of 3.7×10^{-18} at the nominal operational trap depth. Uncertainty in the trap depth determination produces an additional uncertainty ranging from 8.0×10^{-19} to 1.9×10^{-18} and the effective hyperpolarizability coefficient, β^*, contributes an additional uncertainty of 8.9×10^{-19}. For the second wavelength—used only on the final comparison day—the light shift evaluation taken on the same day contributes an uncertainty of 6.4×10^{-18}.

Third, the quoted blackbody radiation uncertainty in ref. [7] has been increased compared to the ratio measurements reported here owing to ageing of both thermistor calibrations (2 mK) and resistance measurement calibrations (3.9 mK). Apart from these calibration uncertainties, the thermal environment control detailed in ref. [7] is identical to the one used in this work with an average temperature difference between clock comparison data and that in ref. [7] of −5 mK. During the clock comparison data campaign, the standard deviation of the model temperature on any given day was typically higher than that observed in ref. [7]. To account for this effect, we include an increased temperature uncertainty that varies from a minimum of 900 μK to a maximum of 12 mK. As a result of the aforementioned effects, the uncertainty in the determination of the blackbody radiation shift is larger than the 2×10^{-19} level of ref. [7], moving to a range that varies day-by-day from 3.6×10^{-19} to 8.9×10^{-19}.

Finally, ref. [7] utilizes an improved fibre phase noise cancellation scheme developed for the optimization of stability transfer of cavity-stabilized probe laser light to the atoms[32]. As an added benefit, this scheme dramatically reduces shifts due to the clock AOM (acousto-optic modulator) phase chirp because these phase transients are actively cancelled by the fibre noise servo and occur when the laser frequency is at large detuning from resonance. However, this improved scheme was not yet implemented in the work presented here, and therefore a shift uncertainty of 1.2×10^{-18} is included.

Yb optical lattice clock

During each comparison day, the Yb optical lattice clock was operated at the nominal conditions described in ref. [8]. Before each comparison, operational parameters were carefully measured to confirm that the systematic shifts and uncertainty were consistent with ref. [8].

Recently, an independent experimental effort[57] measured the magnetic dipole/electric quadrupole polarizability in Yb to be larger than earlier theoretical calculations (refs. [58,59] and M. S. Safronova and S. G. Porsev, personal communication). While additional effort will be required to resolve this discrepancy, we note that the larger polarizability would imply an additional lattice light shift of approximately 3×10^{-18}, which is below the uncertainty of the ratios reported here.

To verify the systematic effects of the Yb optical lattice clocks at NIST, two similar systems, Yb-1 and Yb-2, were developed. For all of the optical comparisons, except for 23 March 2018, the Yb-1 clock system was used. On 23 March 2018, the Yb-2 clock system, run under identical conditions to Yb-1, was used for optical frequency comparisons. The frequency consistency of the Yb-1 and Yb-2 systems has been evaluated as $(-7 \pm 9) \times 10^{-19}$ in ref. [8], and thus does not contribute a substantial uncertainty to the optical ratio.

We note that all the optical frequency ratio data contributing to the measurement described here were collected simultaneously with the data used to determine Yb clock absolute frequency reported in ref. [49].

Ratio uncertainties from χ^2 statistics

To evaluate the final ratios and their uncertainties, the data collected on each day were treated as independent measurements for two reasons.

First, individual days were operationally different from one another, resulting in both measurement stability and some systematic effects that varied day by day (details in Supplementary Tables 1–3). Second, the data were sampled unevenly, with dead-time lasting from minutes to months. Under these conditions, standard tools in stability analysis such as the Allan deviation do not accurately capture the statistical uncertainty except in the case of white frequency noise. While data taken within each day exhibit white frequency noise statistics (Fig. 2a), the same was not observed when data were concatenated across measurement days (see Extended Data Fig. 2).

Scatter in the data from day to day can be quantified using the weighted standard deviation $\text{WSD} = \left(\frac{N \sum_{i=1}^{N} w_i (x_i - \bar{x})^2}{(N-1) \sum_{i=1}^{N} w_i} \right)^{1/2}$, where x_i is the daily ratio, $\bar{x}$ is the weighted mean with weights $w_i = 1/\sigma_i^2$, σ_i is the daily statistical uncertainty and N is the total number of measurements. Note that σ_i includes contributions from the ratio instability and, in the case of the Sr ratios, statistical uncertainty due to the atomic density shift, which was evaluated daily (see Supplementary Table 3), but does not include other systematic effects. For these data WSD = $\{1.7, 0.6, 1.1\} \times 10^{-17}$ for Al$^+$/Yb, Al$^+$/Sr and Yb/Sr, respectively. One commonly used approach to evaluate the statistical error in the presence of excess scatter is the standard error of the mean inflated by the Birge ratio ($\sqrt{\chi_{\text{red}}^2}$, where $\chi_{\text{red}}^2 = 1/(N-1) \times \sum_{i=1}^{N} (x_i - \bar{x})^2/\sigma_i^2$ is the reduced-χ^2 value)[60]. This is shown as the weighted standard error (WSE) in Extended Data Table 3. In the case of Al$^+$/Sr with $\chi_{\text{red}}^2 < 1$, we use the standard error without deflating by $\sqrt{\chi_{\text{red}}^2}$. The total uncertainty from the combined data can then be estimated by summing the WSE in quadrature with uncertainties due to systematic effects.

The data in Fig. 2b–d have $\chi_{\text{red}}^2 = \{1.5, 0.2, 6.0\}$ for Al$^+$/Yb, Al$^+$/Sr and Yb/Sr, respectively. In the case of the Al$^+$ ratios, with the σ_i ranging from 7.3×10^{-18} to 5.4×10^{-17} depending primarily on the duration of the measurement, the χ_{red}^2 values are of the order of one or lower. Conversely, the Yb/Sr measurements had σ_i as low as 2.3×10^{-18} in a single day, revealing excess scatter beyond statistical effects alone. We interpret this as evidence for systematic frequency shifts that appear constant on a particular day but vary between days.

Long-term stability

A plot of the long-term stability of the ratios is given in Extended Data Fig. 2. This is generated by binning all of the measurement data into 10-s intervals, then concatenating multiple days of data together, ignoring dead-time, and computing the overlapping Allan deviation. Care should be taken when interpreting these plots because data were acquired in short segments over many months. However, it can be seen that the instability of the Al$^+$ ratios is consistent with white noise for timescales from 100 s to the longest averaging times at 30,000 s. For the Yb/Sr ratio, with resolution approaching 1×10^{-18}, clear effects from fluctuating systematic shifts appear as a departure from white-noise averaging at larger bin sizes.

Comprehensive Bayesian model

Whereas metrics such as those described above have been commonly used for individual frequency ratio analyses, based on the noise character of the measurements involved, we developed a comprehensive Bayesian approach for the computation of each of the three frequency ratio values and their associated uncertainties. This allowed us to treat all three frequency ratios in an equivalent way based on our best knowledge of their noise properties. Additionally, such an approach provides not only an estimate of the ratio uncertainty but also an estimate of the uncertainties of other model outputs such as an additional between-day variability not included in the clocks' evaluations.

We detail ratio-specific models in Supplementary Information, but each can be summarized using the following framework. We define μ as the true unknown value of the ratio, expressed in all cases below as an offset from the ratio of frequency values currently recommended by CIPM[15]. Systematic effects that have constant magnitude across the measurement campaign (including many atomic effects, network effects and the geopotential) cause us to measure instead a ratio η, shifted from μ, where

$$\eta | \mu, \sigma_{\text{C}} \sim N(\mu, \sigma_{\text{C}}^2). \tag{1}$$

The vertical bar can be read as 'given', '~' means 'is distributed as', and $N(m,v)$ denotes a normal distribution with mean m and variance v. Here σ_{C}^2 is the sum over squared uncertainty contributions due to static systematic effects (reported in Extended Data Table 3). This η will be the same for every individual ratio measurement taken over the entire measurement campaign.

On any given day of ratio measurements, we do not directly measure this shifted value. Rather, the daily ratio measurement x_i for day $i = 1, ..., I$ will be affected by random effects that vary from day to day. Some systematic effects may be correlated from day to day but scaled by different values corresponding to the operating conditions. For example, uncertainty in the sensitivity of a clock frequency to an electromagnetic field may be scaled by a known field at which the clock was operated on a particular day. We make the conservative assumption that these systematic effects are fully correlated across all days of measurement by defining systematic effects $\alpha \sim N(0,1)$ and $\beta \sim N(0,1)$, one for each clock, where α and β are fixed across the measurement campaign. These systematic effects shift the measured daily ratios from η. The magnitude of the effect is scaled by daily vectors **a** and **b**. Each component a_i or b_i defines the magnitude of the clock uncertainty for day i (see Supplementary Information).

The daily ratio measurement x_i will also be affected by measurement instability and any other statistical effects that are not correlated from day to day, such as the density shift for the Sr clock. The variance of these known statistical effects is σ_i^2. We also allow for any potential systematic shifts or statistical fluctuations that are not accounted for in the evaluations of the clocks. This between-day variability, ξ^2, models any excess variation between measurements taken on different days. Combining the known correlated systematic effects, the known statistical effects, and any unknown excess between-day variability, the ratio measurements x_i can be modelled as,

$$x_i | \eta, \alpha, \beta, \mathbf{a}, \mathbf{b}, \xi, \boldsymbol{\sigma} \sim N(\eta + a_i \alpha + b_i \beta, \sigma_i^2 + \xi^2). \tag{2}$$

We use this framework to develop a specific model for the measurements of each ratio. To estimate the parameters of these models, we use a Bayesian approach[38] similar to that detailed in ref. [39]. In a Bayesian analysis, we are interested in the posterior probability of the parameters given data $p(\boldsymbol{\theta}|\mathbf{y})$, where $\boldsymbol{\theta} = (\mu, \eta, \alpha, \beta, \xi)$ is a vector of unknown parameters and $\mathbf{y} = (\mathbf{x}, \boldsymbol{\sigma}, \mathbf{a}, \mathbf{b}, \sigma_{\text{C}})$ is a vector of the observed data. From Bayes' rule,

$$p(\boldsymbol{\theta}|\mathbf{y}) \propto p(\boldsymbol{\theta}) \times p(\mathbf{y}|\boldsymbol{\theta}).$$

Here $p(\boldsymbol{\theta})$ is the prior distribution, and $p(\mathbf{y}|\boldsymbol{\theta})$ is the likelihood. The prior distribution $p(\boldsymbol{\theta})$ is the product of individual prior distributions for each of the unknown parameters.

For all three ratio models, we assume a priori $\mu \times 10^{18} \sim N(0, 10^5)$, which is a relatively flat distribution that conveys little prior knowledge about the value of the true ratio. For the between-day variability $\xi (\times 10^{18})$, we assume a half-Cauchy prior distribution centred at zero and with a scale of 1,000 to make the prior distribution diffuse, shown in Extended Data Fig. 3b. We tested the sensitivity of the results to this choice of prior distribution and saw little effect for reasonably diffuse prior distribution options.

We use Markov chain Monte Carlo (MCMC) to sample from the posterior distribution, implemented using the R package R2jags[61], using 10^9

Article

total iterations for the MCMC with 10^7 burn-in iterations. This means we discard the first 10^7 samples, where the Markov chain is still converging. We thin the resulting chains to reduce autocorrelation in the samples by saving only every 250th sample. The results are thus based on 3,960,000 samples from the posterior distribution. To check for convergence of the Markov chains, we visually inspect trace plots of the posterior samples, as seen in Extended Data Fig. 3c, and use the convergence diagnostic suggested by ref. [62].

We plot the resulting posterior distributions for our parameters of interest, μ and the between-day variability ξ. These are shown for the three ratios in Extended Data Fig. 3a. The mean, standard deviation and 95% quantiles of the posterior samples give us the estimates, uncertainties and credible intervals reported in Extended Data Table 2.

Correlation analysis

Because many of the measurements described here were taken with three clocks running simultaneously, a statistically significant linear relationship between the daily measurements of two ratios could identify the source of between-day variability. To test this, we use errors-in-variables regression[63,64] (Extended Data Fig. 4). Statistical fluctuations arising from the overlapping uptime of the clock frequency that is shared between the x and y axes are perfectly correlated, so uncertainty from this is removed from the total statistical uncertainties of the ratios. Specifically, the total statistical variance for each ratio, σ_i^2, is separated into independent contributions from the non-common-mode clock (B) and the overlapping and non-overlapping portions of the clock which is common to both axes (A): $\sigma_i^2 = \sigma_{A,over}^2 + \sigma_{A,non}^2 + \sigma_B^2$. From the measured ratio stability on each day the instability of the overlapping portion of clock B is estimated by $s_A/\sqrt{T} \times \sqrt{t/T}$, where s_A is the single clock stability, T is the daily ratio data length, and t is the duration of the overlapping data between the two ratios. This is subtracted from the total uncertainty, yielding an estimate of the uncorrelated variance, $\sigma_{A,non}^2 + \sigma_B^2$. These error bars allow us to treat the x and y fluctuations independently. The confidence intervals for the three fitted slope parameters each contain zero, meaning that the small number of measurements do not provide sufficient resolution to identify statistically significant linear relationships between ratios.

Dark-matter constraints

Analysis of the optical frequency ratio data closely follows previous work using atomic spectroscopy to establish bounds on the coupling parameter in a model of ultralight bosonic dark matter[9,10]. In this model, a dark-matter particle with Compton frequency ω_C couples through the apparent values of fundamental constants to produce a sinusoidal perturbation to the measured ratio $(R(t) - R_0)/R_0 = \delta_R \sin(\omega_C t + \theta)$. Here, R_0 is the time-averaged ratio value, δ_R is the fractional amplitude of its oscillation and θ is an unknown phase. We consider Compton frequencies $1/(20T_{max}) < \omega_C/2\pi < 1/100$ s, where T_{max} is the period between the first and last measurements in the full time series and the cutoff at a 100-s period is well above the servo time constants of ~10 s, thus eliminating sensitivity of the ratios to variations in the length of the optical cavities[65,66]. For ratio $R(t) = \nu_1(t)/\nu_2(t)$, the sensitivity to fractional changes in the fine-structure constant, α_{FS}, is given by $\Delta K = |K_1 - K_2|$, where coefficient values ($K_{Al^+} = 0.008, K_{Sr} = 0.06, K_{Yb} = 0.31, K_{Hg^+} = -2.9$) are taken from ref. [1]. By fitting a sinusoidal model including a constant offset to the time-series ratio data, we obtain upper bounds on δ_R at 95% confidence. The analysis routine has been tested against analytical results from a white noise model and verified by injecting artificial

signals and confirming that their amplitudes are faithfully reproduced in the spectrum. These bounds are plotted in Fig. 4 in terms of δ_R and the coupling parameter $d_e = 4.2 \times 10^{30} \delta_R m_\phi/\Delta K$, where m_ϕ is in eV, which is normalized to a gravitational-strength interaction[9], assumes a local dark-matter density of 0.4 GeV cm^{-3} and takes into account stochastic fluctuations in dark-matter field amplitude with a uniform rescaling by a factor of 3.0 (ref. [53]). As suggested in ref. [53], we have increased the value of previous bounds to account for the probability distribution of the dark-matter field amplitude.

Data availability

The data presented here are available from the corresponding authors on reasonable request.

55. Ma, L.-S., Jungner, P., Ye, J. & Hall, J. L. Delivering the same optical frequency at two places: accurate cancellation of phase noise introduced by an optical fiber or other time-varying path. *Opt. Lett.* **19**, 1777–1779 (1994).
56. Newbury, N. R., Williams, P. A. & Swann, W. C. Coherent transfer of an optical carrier over 251 km. *Opt. Lett.* **32**, 3056–3058 (2007).
57. Nemitz, N., Jørgensen, A. A., Yanagimoto, R., Bregolin, F. & Katori, H. Modeling light shifts in optical lattice clocks. *Phys. Rev. A* **99**, 033424 (2019).
58. Brown, R. C. et al. Hyperpolarizability and operational magic wavelength in an optical lattice clock. *Phys. Rev. Lett.* **119**, 253001 (2017).
59. Katori, H., Ovsiannikov, V. D., Marmo, S. I. & Palchikov, V. G. Strategies for reducing the light shift in atomic clocks. *Phys. Rev. A* **91**, 052503 (2015).
60. Mohr, P. J., Newell, D. B. & Taylor, B. N. Codata recommended values of the fundamental physical constants: 2014. *Rev. Mod. Phys.* **88**, 035009 (2016).
61. Su, Y.-S. & Yajima, M. R2jags: using R to run 'JAGS'. https://cran.r-project.org/web/packages/R2jags/index.html (2015).
62. Geweke, J. Evaluating the accuracy of sampling-based approaches to calculating posterior moments. In *Bayesian Statistics 4: Proceedings of the Fourth Valencia International Meeting* (eds Bernado, J. M. et al) 641–649 (Clarendon, 1992).
63. Fuller, W. A. *Measurement Error Models* (Wiley & Sons, 1987).
64. Carroll, R. J., Ruppert, D., Stefanski, L. A. & Crainiceanu, C. M. *Measurement Error in Nonlinear Models — A Modern Perspective* 2nd edn (Chapman & Hall/CRC Texts in Statistical Science) (CRC Press, 2006).
65. Wcisło, P. et al. New bounds on dark matter coupling from a global network of optical atomic clocks. *Sci. Adv.* **4**, eaau4869 (2018).
66. Kennedy, C. J. et al. Precision metrology meets cosmology: improved constraints on ultralight dark matter from atom-cavity frequency comparisons. *Phys. Rev. Lett.* **125**, 201302 (2020).

Author contributions All authors contributed to the design of the experiment, collection of data and revision of the manuscript. During the measurement campaign, Al$^+$ clock operation was conducted by S.M.B., J.-S.C., D.B.H. and D.R.L.; Sr clock operation was conducted by T.B., S.L.B., D.K., C.J.K., W.R.M., E.O., J.M.R., L.S. and J. Ye; Yb clock operation was conducted by K.B., R.J.F., Y.S.H., A.D.L., W.F.M., D.N., S.A.S. and X.Z.; comb metrology laboratory operation was conducted by T.M.F. and H.L.; maser operation and comparison with UTC-NIST was conducted by T.E.P., S.R., J.A.S. and J. Yao; O-TWTFT system operation including the free-space link was conducted by M.I.B., J.-D.D., S.A.D., I.K., N.R.N., L.C.S. and W.C.S.; network interconnections excluding the free-space link were maintained by H.L., W.R.M., E.O. and J.M.R. Ratio data analysis and preparation of the manuscript were performed by T.M.F., D.B.H., D.K., C.J.K., A.K., H.L., L.C.S. and X.Z.

Extended Data Fig. 1 | Diagram of the Boulder Atomic Clock Optical Network (BACON). The Al⁺ ion optical clock (blue shaded area), the Yb optical lattice clock (orange shaded area), the Er:fibre comb (light grey shaded area) and the Ti:S comb (light grey shaded area) are located in Building 81 of NIST. The Sr optical lattice clock (pink shaded area) is located in the basement of JILA. The free space link (grey shaded area) includes two parts (split by the dashed line): one part is located in the NIST Building 1 penthouse and another part is located at the 11th floor of the Gamow tower at the University of Colorado. The Er:fibre comb and the Ti:S comb at NIST are locked to the Yb optical clock. The Er:fibre comb in the Sr optical clock lab is locked to the Si cavity and is used to transfer the Si cavity stability to the Sr clock laser. Free space Er:fibre combs are locked to the Yb optical clock through the Er:fibre comb at NIST and the Sr optical clock through the Si cavity, respectively. All AOM frequencies in the network are referenced to a hydrogen maser at NIST, which is transferred to JILA through an optical fibre link. The frequency shifts of optical clocks due to calibrated systematic effects are added to the optical frequency ratio calculations in post-processing. FNC, fibre-noise cancellation. In key at bottom right: f_0, carrier-envelope offset frequency; f_b, beatnote frequency; Tis, Ti:sapphire; fsp, free space.
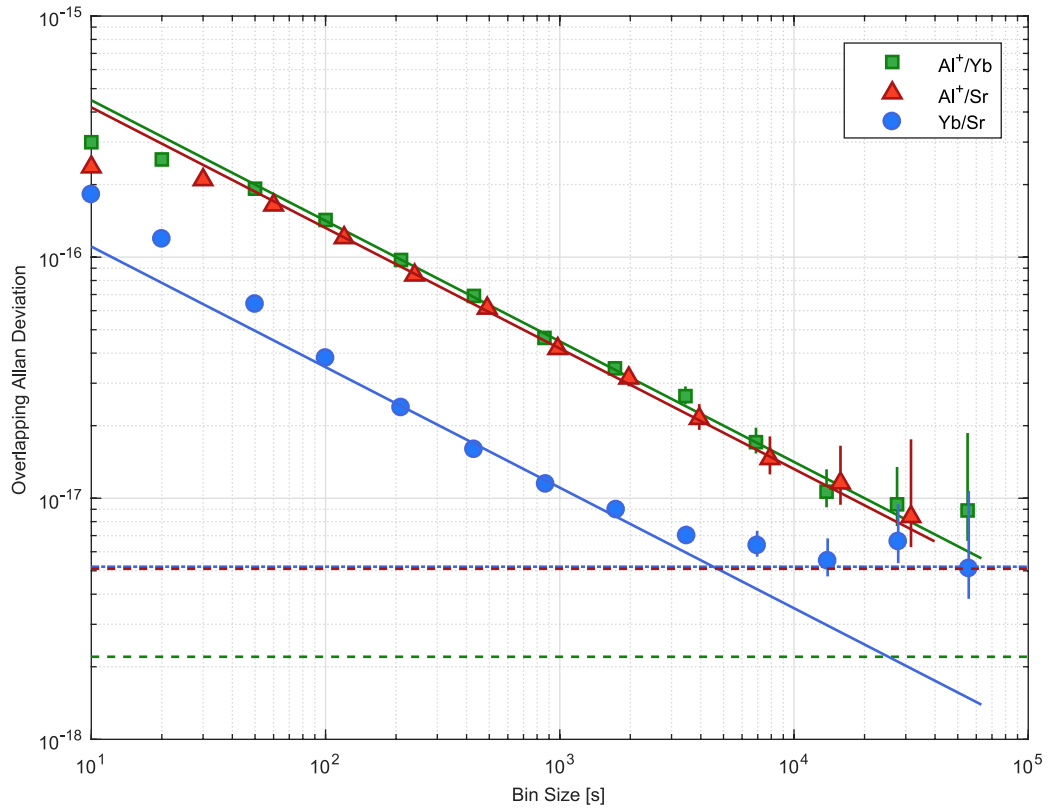
Extended Data Fig. 2 | Long-term stability of concatenated ratio data as characterized by the overlapping Allan deviation. The data plotted include all measurements that were taken at the nominal operating conditions over the course of the measurement campaign with total measurement durations as follows: 165,240 s, 94,760 s and 167,140 s for Al⁺/Yb, Al⁺/Sr and Yb/Sr, respectively. For the Al⁺/Yb ratio, in addition to the data that contributed to the final ratio, we include two extra days of data (27 February 2018 and 2 March 2018) that were used in the evaluation of the Al⁺ second-order Zeeman shift as described in ref. [6]. Although acquired in very similar experimental conditions, these datasets are excluded from frequency ratio estimate to avoid statistical correlation between the systematic shift evaluation and the frequency ratio measurement. Because the data were taken in short segments over many months, the time series is dominated by periods of dead-time such that the noise spectrum cannot be identified unambiguously. Fits (solid lines) use a white frequency noise model: $\sigma_y(\tau) = \sigma_{1s}/(\tau/s)^{1/2}$, where σ_{1s} is the extrapolated 1-s instability. These include all data beyond the $\tau = 100$ s bin size with weights equal to the number of bins contributing to each point. Although it is not directly related to the stability, for reference, the total systematic uncertainty evaluated for each ratio is indicated by a corresponding dashed line. Error bars indicate 68% confidence intervals based on a white frequency noise model.
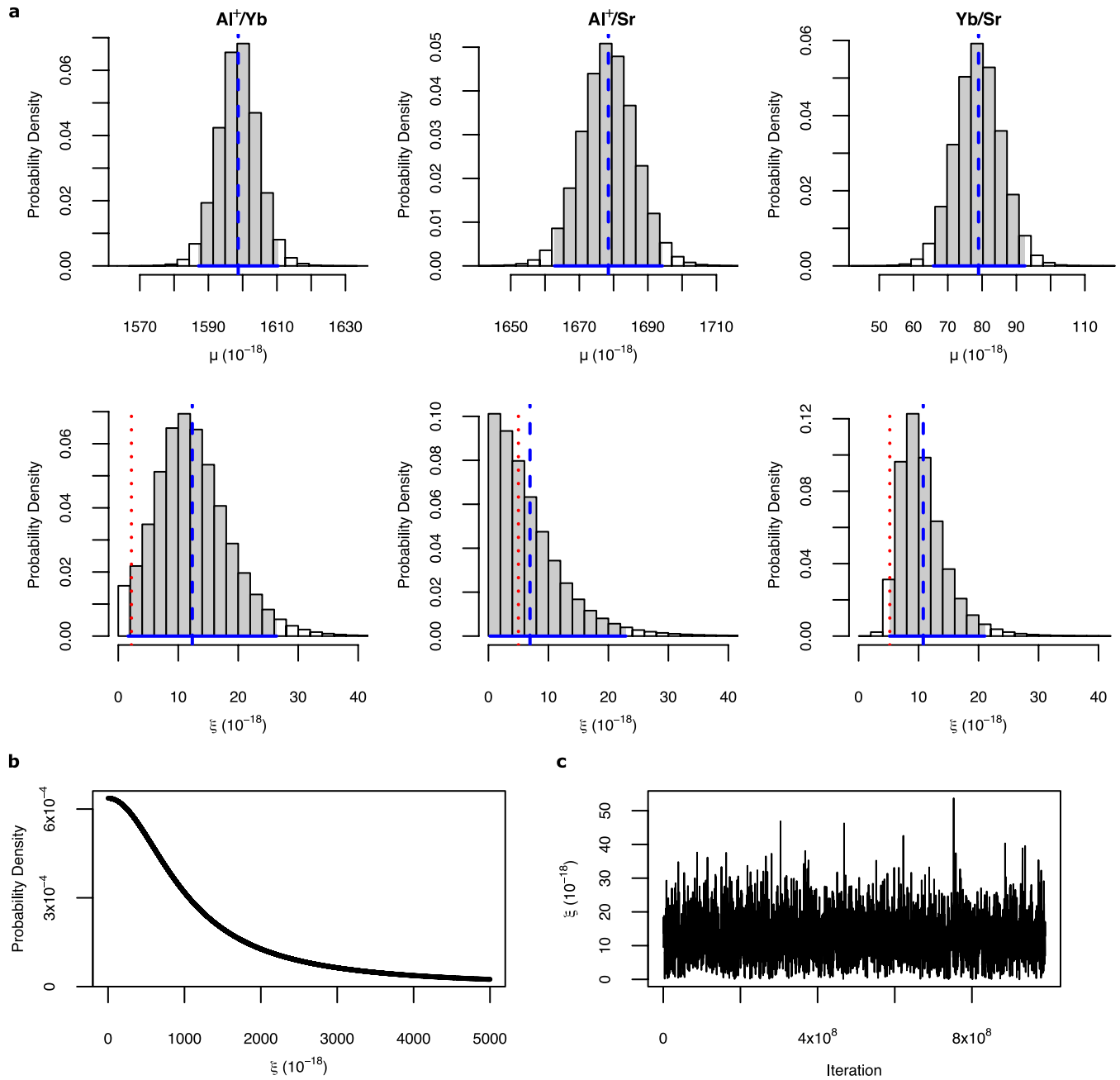
Extended Data Fig. 3 | Results of the Bayesian analysis. a, Posterior distributions for the ratio values μ (top row) expressed here as a fractional offset from the current recommended CIPM values[15], and for the between-day variability ξ (bottom row). Left column, ratio Al⁺/Yb; middle column, ratio Al⁺/Sr; right column, ratio Yb/Sr. The blue dashed lines denote our estimate for these parameters, the posterior mean. The shaded areas and blue lines on the bottom of each plot denote the 95% credible intervals and the red dotted lines denote the static uncertainties due to systematic effects. The posterior

distributions for ξ have mass concentrated on values closer to zero and widths comparable to their means. More comparison days would be needed to further constrain these parameters. **b**, Prior distribution for ξ. **c**, Trace plots for the between-day variability ξ for the Al⁺/Yb measurements. The x axis is the MCMC iteration number (plotting every 1,000th sample) and the y axis is the value of the parameter. Trace plots are used as a convergence diagnostic for MCMC; these plots show that the chains are mixing well.
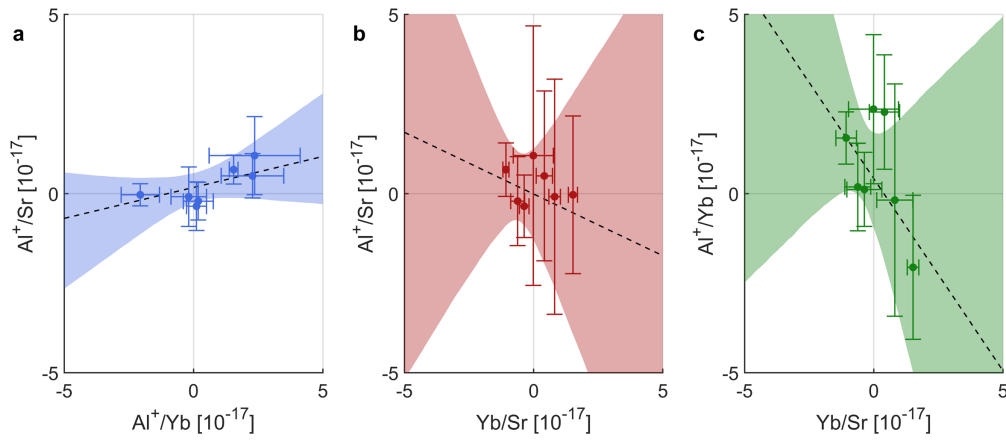
Extended Data Fig. 4 | Correlation analysis for daily measurements of all ratio pairs. a, Al$^+$/Sr versus Al$^+$/Yb; **b**, Al$^+$/Sr versus Yb/Sr; and **c**, Al$^+$/Yb versus Yb/Sr. Data are offset by their mean and error bars account for known correlations between the x and y uncertainties as described in the Methods. All days with simultaneous ratio measurements from each pair are plotted. There is no statistically significant linear relationship between these ratios, indicating that the present clock data, with only seven overlapping days of data, are not precise enough to identify a source of daily fluctuations. The slopes (dashed black lines) and 95% confidence intervals (shaded areas) for the three plots are: **a**, 0.17 (−0.08, 0.53), **b**, −0.34 (−1.90, 1.19), and **c**, −1.07 (−3.09, 0.72).

Extended Data Table 1 | Clock operating parameters

Parameter	^{27}Al$^+$	^{171}Yb	^{87}Sr
Number of atoms	1	1000	2000
Clock transition	$^1S_0 \leftrightarrow {}^3P_0$	$^1S_0 \leftrightarrow {}^3P_0$	$^1S_0 \leftrightarrow {}^3P_0$
Clock wavelength [nm]	267	578	698
Excited-state lifetime [s]	20.6(1.4)	20(2)	120(3)
Nuclear spin	5/2	1/2	9/2
Probe time [ms]	150	560	500
Atom temperature [μK]	≈ 100	≈ 1	≈ 2
Limiting systematic shifts	Micromotion time-dilation	Blackbody radiation, Lattice light	Lattice light
Servo time constant [s]	14	10	10
Probe duty cycle [%]	50	65	45

Article

Extended Data Table 2 | Numerical results for μ and ξ

Parameter	Ratio	Estimate	Uncertainty	68% CI	95% CI
μ (10^{-18})	Al^+/Yb	1598.7	5.9	(1593.1, 1604.3)	(1587.1, 1610.3)
Ratio expected	Al^+/Sr	1678.5	8.0	(1670.7, 1686.2)	(1662.8, 1694.2)
value	Yb/Sr	79.0	6.8	(72.3, 85.6)	(65.8, 92.5)
ξ (10^{-18})	Al^+/Yb	12.3	6.2	(6.3, 18.2)	(1.6, 26.4)
Between-day	Al^+/Sr	6.9	6.3	(1.6, 12.0)	(0.2, 22.9)
variability	Yb/Sr	10.8	4.2	(7.1, 14.3)	(5.1, 21.1)

Results for μ (in units of 10^{-18}), expressed here as a fractional offset from the current recommended CIPM values[15], and for the between-day variability ξ (in units of 10^{-18}), are based on 3,960,000 samples from the posterior distributions. The estimate is the mean of these samples, the uncertainty is the standard deviation, and the 68% and 95% credible intervals come from the 68% and 95% quantiles of this sample.

Extended Data Table 3 | Fractional ratio uncertainties

		$\mathrm{Al}^+/\mathrm{Yb}\ \left(10^{-18}\right)$	$\mathrm{Al}^+/\mathrm{Sr}\ \left(10^{-18}\right)$	$\mathrm{Yb}/\mathrm{Sr}\ \left(10^{-18}\right)$
	Sr	-	4.8	5.0
	Yb	1.4	-	1.4
Systematic	Al^+	1.7	1.5	-
	Network (σ_N)	0.3	0.5	0.5
	Geopotential (σ_G)	0.2	0.4	0.4
Statistical	$\mathrm{WSE} = \sqrt{\chi^2_{\mathrm{red}}\left(\sum_i \frac{1}{\sigma_i^2}\right)^{-1/2}}$	$4.3\ \left(\chi^2_{\mathrm{red}}=1.5\right)$	$4.8^a\ \left(\chi^2_{\mathrm{red}}=0.2\right)$	$3.7\ \left(\chi^2_{\mathrm{red}}=6.0\right)$
Quadrature Sum (sys. and stat.)		**4.8**	**7.0**	**6.4**
Comprehensive Bayesian model		**5.9**	**8.0**	**6.8**

Contributions to measurement uncertainty due to systematic effects (sys.) from each clock (first three rows) were evaluated separately for all ratios as a weighted mean of the daily uncertainties. These are weighted, according to the statistical uncertainty, as $1/\sigma_i^2$. Additive uncertainty from the optical network (fourth row) and from the geopotential (fifth row) was determined by a loop-back measurement and a geodetic survey, respectively. We compare an estimate of the total uncertainty (seventh row) calculated from the weighted standard error (WSE, stat.; sixth row) and uncertainty in systematic effects to the results of the comprehensive Bayesian model, which returns a distribution of ratio values whose standard deviation is given in the last row.
^{a}To avoid underestimating uncertainty in the under-scattered $\mathrm{Al}^+/\mathrm{Sr}$ ratio ($\chi^2_{\mathrm{red}} = 0.2$), the standard error of the mean, ignoring χ^2_{red}, is used.